

Impact of Manganese on Primary Hippocampal Neurons From Rodents

Alexia Daoust,^{1,2} Yasmina Saoudi,^{1,2} Jacques Brocard,^{1,2} Nora Collomb,^{1,2} Cécile Batandier,⁴ Mariano Bisbal,^{1,2} Murielle Salomé,³ Annie Andrieux,^{1,2} Sylvain Bohic,^{1,2,3} and Emmanuel L. Barbier^{1,2*}

ABSTRACT: Manganese-enhanced magnetic resonance imaging (MEMRI) is a powerful tool for *in vivo* tract tracing or functional imaging of the central nervous system. However Mn^{2+} may be toxic at high levels. In this study, we addressed the impact of Mn^{2+} on mouse hippocampal neurons (HN) and neuron-like N2a cells in culture, using several approaches. Both HN and N2a cells not exposed to exogenous $MnCl_2$ were shown by synchrotron X-ray fluorescence to contain 5 mg/g Mn. Concentrations of Mn^{2+} leading to 50% lethality (LC50) after 24 h of incubation were much higher for N2a cells (863 mM) than for HN (90 mM). The distribution of Mn^{2+} in both cell types exposed to Mn^{2+} concentrations below LC50 was perinuclear whereas that in cells exposed to concentrations above LC50 was more diffuse, suggesting an overloading of cell storage/detoxification capacity. In addition, Mn^{2+} had a cell-type and dose-dependent impact on the total amount of intracellular P, Ca, Fe and Zn measured by synchrotron X-ray fluorescence. For HN neurons, immunofluorescence studies revealed that concentrations of Mn^{2+} below LC50 shortened neuritic length and decreased mitochondria velocity after 24 h of incubation. Similar concentrations of Mn^{2+} also facilitated the opening of the mitochondrial permeability transition pore in isolated mitochondria from rat brains. The sensitivity of primary HN to Mn^{2+} demonstrated here supports their use as a relevant model to study Mn^{2+} -induced neurotoxicity. © 2014 Wiley Periodicals, Inc.

KEY WORDS: manganese; MEMRI; X-ray synchrotron; hippocampal neurons; mitochondria

INTRODUCTION

Manganese (Mn^{2+}) is an essential metal ion for brain functions (Aschner et al., 2006). For example, it is a cofactor for several critical enzymes in the brain and is also involved in the synthesis of amino acids and lipids as well as certain neurotransmitters, including dopamine and

serotonin (Golub et al., 2005). However, at high levels, Mn^{2+} is toxic for the central nervous system. In humans, chronic Mn^{2+} exposure in the workplace results in manganism, a psychiatric and motor disorder characterized by Parkinsonian-like symptoms (Stredrick et al., 2004; Josephs et al., 2005).

Mn^{2+} has paramagnetic properties and can be used as a contrast agent for manganese-enhanced magnetic resonance imaging (MEMRI) (Koretsky and Silva, 2004). In addition, by way of its divalency, Mn^{2+} can substitute calcium by entering active neurons through voltage-gated calcium (Ca^{2+}) channels (Narita et al., 1990) where it is transported by microtubule-dependent axonal transport or through synapses (Paotler, 2004). Mn^{2+} is thus a unique contrast agent to trace neuronal connections *in vivo*, to perform functional studies or to enhance visualization of brain cytoarchitecture (Silva and Bock, 2008).

In MEMRI, the toxicity of focal Mn^{2+} injections is less severe than that of systemic injections: a focal injection does not impact the digestive and cardiac functions, and focal doses are lower than systemic ones (Silva and Bock, 2008). However, several studies showed that an intra-cerebral injection of Mn^{2+} may be toxic for neurons and glial cells (Canals et al., 2008; Ponzoni, 2012). Indeed, rats intra-cerebrally injected with Mn^{2+} (200 nL, 100 mM) displayed neuronal toxicity and clear astrogliosis (Canals et al., 2008). Mn^{2+} has been shown to accumulate within mitochondria and adversely affect mitochondrial function (Heron et al., 2001; Morello et al., 2008). Clinical and experimental evidence highlights Mn^{2+} as a mitochondrial disrupting agent that thereby impairs cerebral energy metabolism leading to energy failure (Malecki, 2001; Malthankar et al., 2004; Zwingmann et al., 2004). In differentiated PC12 cells, Carmona et al. (Carmona et al., 2010) observed that Mn^{2+} lowers the total cellular iron (Fe) content and that the Golgi apparatus plays an important role in the cellular detoxification of Mn. An impact of Mn^{2+} on the homeostasis of essential trace elements such as divalent and trivalent iron (Fe^{2+} / Fe^{3+}) and divalent calcium (Ca^{2+}) has also been reported (Drapeau and Nachshen, 1984; Kwik-Urbe et al., 2003; Fitsanakis et al., 2010; Daoust et al., 2013).

The exact mechanism(s) of Mn^{2+} neurotoxicity remains unknown. Given the interest of Mn^{2+} as a

¹ Inserm, U836, Grenoble, France; ² Université Grenoble Alpes, Grenoble Institut des Neurosciences, Grenoble, France; ³ European Synchrotron Radiation Facility (ESRF), Grenoble, France; ⁴ Laboratoire de Bioénergétique Fondamentale et Appliquée, Grenoble, France

Additional Supporting Information may be found in the online version of this article.

*Correspondence to: Emmanuel L. Barbier, Grenoble Institut des Neurosciences – U836, Team 5, Functional NeuroImaging and Brain Perfusion, UJF Site santé – BP 170, 38042 Grenoble cedex 9, France. E-mail: emmanuel.barbier@ujf-grenoble.fr

Accepted for publication 24 January 2014.

DOI 10.1002/hipo.22252

Published online 6 February 2014 in Wiley Online Library (wileyonlinelibrary.com).

contrast agent to probe neuron function with MRI and in the longitudinal study of hippocampal structure and function, understanding its adverse effects on neurons is crucial to determine the potential toxicity of focal Mn^{2+} injections in the brain. To address this point, we studied the effect of Mn^{2+} exposure on primary hippocampal neurons (HN) using several techniques: synchrotron X-ray fluorescence (SR-XRF) nanoprobe, immunofluorescence microscopy, evaluation of mitochondrial permeability transition pore (MPTP) opening, and analysis of mitochondria dynamics. In addition to revealing the impact of Mn^{2+} at the subcellular level, our data highlight the difference in Mn^{2+} toxicity between a primary culture of neurons and differentiated Neuro2a (N2a) neuroblastoma cells. To our knowledge, this is the first report describing the distribution and the impact of Mn^{2+} at the subcellular level in HN.

METHODS

Cell Preparation

Briefly, hippocampus brain tissue from E18.5 (embryonic day 18.5) mice was removed and digested in 0.25% trypsin in Hepes-HBSS (5.3 mM KCl, 0.44 mM KH_2PO_4 , 137.9 mM NaCl, 0.34 mM NaH_2PO_4 , 5.56 mM glucose, Invitrogen, France) at 37°C for 15 min. After manual dissociation, HN were plated at a concentration of 7×10^4 cells cm^{-2} on poly-L-lysine (1 mg mL^{-1} poly-L-lysine hydrobromide, Sigma-Aldrich)-coated coverslips (Fig. 1) in DMEM+10% fetal bovine serum (FBS). One hour after plating, the medium was changed to Neurobasal containing B27 (Invitrogen, France).

N2a cells (mouse neuroblastoma, CCL-131, ATCC, Manassas, VA) were maintained in DMEM 1X (with GlutaMAX, 4500 mg L^{-1} D-glucose, sodium pyruvate, Invitrogen, France) supplemented with 10% FBS, 1% non-essential amino-acids (NEAA) and 100 U mL^{-1} penicillin and streptomycin (PS).

These cells were cultured at 2.4×10^4 cells cm^{-2} and split every 3–4 days. Differentiation of N2a cells was induced by 5 μM retinoic acid (98% powder, Sigma-Aldrich, France). After 24 h in the differentiation medium, N2a differentiated into neuron-like cells with regards morphological and biological criteria (Olmsted et al., 1970).

HN and N2a cells were grown at 36.5°C in a humidified atmosphere with 5% CO_2 .

Toxicity Assay

Manganese cytotoxicity was assessed by thiazolyl blue tetrazolium bromide (MTT M2128, Sigma-Aldrich, St Louis, MO) assays. HN were seeded in 24-well plates at 2.2×10^5 cells per well and N2a cells were seeded in six-well plates at 6×10^4 cells per well. HN was grown for 3 days and N2a cells were differentiated at the 4th day of culture. One day later, $MnCl_2$ ($MnCl_2 \cdot 4H_2O$, M1787, Sigma-Aldrich, St Louis, MO) was added at 200, 500, 800, 1,500 μM for N2a cells as previously described (Higashi et al., 2004; Chtourou et al., 2011), and at 20, 50, 100, 150 μM for neurons according to concentrations found in the brain (Daoust et al., 2013).

The $MnCl_2$ solution was filtered through 0.2- μm membranes before administration to culture medium, giving a pH and osmolarity of 7.3 and 300 mOsm L^{-1} , respectively. Twenty-four hours later, the culture medium was replaced by a solution of 10% MTT diluted in culture medium (5 mg mL^{-1} MTT diluted in PBS with Ca^{2+} and Mg^{2+}) and cells were incubated for an additional 2 h at 36.5°C. The medium was then removed, cells were lysed in DMSO (200 μL for neurons and 1 mL for N2a cells per well), and the solution was transferred to a 96-well plate. The absorbance was measured at 519 nm with a microplate reader (Pherastar plus, BMG Labtech, Germany).

The concentration of $MnCl_2$ leading to 50% lethality (LC50) was determined by linear interpolation of the data (percentage of viable cells as a function of Mn^{2+} concentration).

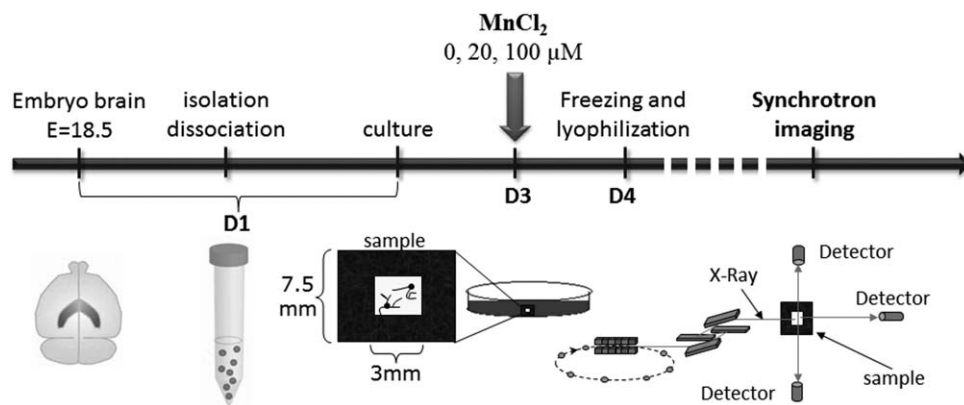


FIGURE 1. Diagram depicting HN sample preparation for SR-XRF imaging. The culture of primary hippocampal neurons (HN) was prepared from neonatal mice ($E = 18.5$). HN were isolated, dissociated and seeded on a silicon nitride window at day 1 (D1). HN was then allowed to grow for 2 days before $MnCl_2$ addition to the medium at day 3 (D3: 0, 20 or 100 μM). At day

4, HN was quickly cryofixed and lyophilized prior to synchrotron imaging (D4). An X-ray fluorescence beam, generated by an electron accelerator, was focused on the sample. Photons ejected during the interaction between the incident beam and the sample, were detected allowing the characterization of each metal according to its specific photon energy.

Synchrotron X-ray Fluorescence Imaging (SR-XRF)

Experiments were carried out at the European Synchrotron Radiation Facility (ESRF) on beamline ID21 (low energy) and ID22NI (high energy) X-ray microscopy end-stations (Bohic et al., 2012).

N2a cells and HN were plated on silicon nitride windows (Gibon et al., 2011) treated beforehand with gelatine 2% for N2a cells or poly-L-lysine 1 mg mL⁻¹ for neurons. Cells were then incubated for 24 h in culture medium supplemented with MnCl₂ at 0, 600, and 1,000 μM for N2a and 0, 20, and 100 μM for HN. The selected concentrations were those surrounding the LC50 of N2a (600 < LC50 < 1,000 μM) and HN (20 < LC50 < 100 μM; see results). The cells were then rinsed to remove salt before being quickly cryofixed at -160°C in isopentane chilled with liquid nitrogen, vacuum freeze-dried at -65°C, and finally stored at room temperature in a desiccator for SR-XRF imaging (Fig. 1). As already described, this protocol preserves the integrity of the cellular morphology and the chemical element distribution in the cells (Carmona et al., 2008).

All HN cells and N2a control cells were analyzed with the X-ray nanoprobe beamline (ID22NI) using an X-ray incident energy of 17.5 keV, an X-ray beam focused to below 100 nm², and a flux of 5 × 10¹¹ photons s⁻¹. The sample was raster-scanned with a step size of 100 nm while the spectrum of the emitted fluorescence was recorded with an energy dispersive silicon drift diode collimated detector (SII Nanotechnology Vortex 50 mm²). The integration time per scan point was 300 ms.

N2a cells exposed to Mn were analyzed with the ID21 end station using an X-ray incident energy of 7.2 keV, an X-ray beam focused to 300 nm × 700 nm, and a flux of 6 × 10¹⁰ photons/s. This lower energy prevents the measurement of X-ray fluorescences of elements above Fe. The sample was raster-scanned with a step size of 300 nm and an integration time of 1–3 s.

Elemental maps were created with PyMCA software (Sole et al., 2007) by fitting pixelwise the recorded spectrum to determine the fluorescence signal of each element. The quantitative evaluation using the fundamental parameter approach provided elemental content i.e. elemental area densities (μg cm⁻²) (Chandler, 1976; Gibon et al., 2011). An average density of ρ = 1.25 g cm⁻³ and the average cell thickness measured by atomic force microscopy (Asylum MFP-3D AFM instrument equipped with acoustic box) were used to calculate the mass fraction (μg g⁻¹ dry weight) for each cell type. Measurements of freeze-dried cells on the Si₃N₄ membranes were obtained in tapping mode under ambient conditions. The average cell thickness was 1.3 ± 0.3 μm for HN (*n* = 10) and 6.6 ± 0.5 μm for N2a cells (*n* = 10).

The NIST standard reference material SRM1577b bovine liver (NIST, Gaithersburg, MD) was used to calibrate experimental parameters. The thin samples prepared required no matrix corrections. Finally, sulfur was used as proxy for proteins (De Jonge et al., 2010) and all elemental concentrations normalized to that of sulfur (S) to correct for possible varia-

tions in slice thickness or in protein amount between samples. Limit of detection of the system can be found elsewhere (De Samber et al., 2013) and was below the elemental concentrations measured in the present work.

Immunofluorescence Microscopy of Hippocampal Neurons

HN was plated 48 h before analysis on glass coverslips coated with poly-L-lysine for immunostaining analysis. MnCl₂ was then added at different concentrations, 24 h after which the neurons were fixed with 3.7% formaldehyde + 0.1% glutaraldehyde in phosphate buffer saline (PBS) for 1 h (all products from Sigma-Aldrich, France). Coverslips were washed six times in PBS and incubated in a NaBH₄ solution (1 mg mL⁻¹ in PBS) for 10 min. Coverslips were washed again three times in PBS and three times in PBS-Triton-X 0.1% before immunostaining in PBS-Tween 0.1% (PBST). Neuronal fibrillar actin (F-actin) was labeled with Alexa Fluor[®] 546 coupled to a phalloidin probe (Life technologies, France) diluted at 1/200 in PBST for 30 min at room temperature. Cells were washed again in PBST and incubated with a mouse monoclonal anti-tubulin α3A1 antibody (dilution 1/5,000 in PBST) for 30 min (Erck et al., 2005). After rinses in PBST, cells were incubated in Alexa 488-coupled anti-mouse secondary antibody (Invitrogen, France) diluted at 1/500 in PBST for 30 min. Neurons were washed three times in PBST and incubated for 2 min in a Hoechst solution (Sigma-Aldrich, France) to label nuclei (dilution 1/2,000 in PBST). Finally, coverslips were briefly rinsed in distilled water, air dried and mounted on glass slides using DAKO fluorescent mounting medium (Dako, France).

Images were acquired with an Axioskop Zeiss microscope (Carl Zeiss, 444 Le Pecq, France) using a 40× oil objective and a Coolsnap ES photometric camera (Roper Scientific, Trenton, NJ) controlled by Metaview software (Universal Imaging, USA).

The quantitative morphological analysis of neurites was performed by scanning each coverslip (two coverslips per condition) with a Leica DMI6000 microscope (Leica, France) using a 40× dry objective and a EMCCD Quantem camera (Roper Scientific, Trenton, NJ) driven by the scan-slide module of Metamorph software (Universal Imaging, USA). Two morphological characteristics of neurites were quantified: their number and their length per neuron.

Mitochondria Dynamics

For dynamic studies of mitochondria, HN were first grown for 3 days in glass-bottom dishes (IWAKI, Dutscher, France) coated with poly-L-lysine 1 mg mL⁻¹ (MnCl₂ was added on the third day). Twenty-four hours after MnCl₂ administration (0, 50, and 100 μM), the culture medium was replaced by fresh neurobasal medium containing MitoTracker Red CMXRos (20 nM; Life technologies, France). After 5 min at 37°C, the dye was replaced by culture medium (37°C) for time lapse experiments to analyze mitochondrial dynamics. HN were placed inside a microscope stage incubator within which air temperature and carbon dioxide concentrations were accurately

controlled in order to keep the media pH constant. Neurons were observed with an inverted microscope Axiovert 200M (Carl Zeiss, France) using an 100× oil objective. During the time-lapse experiments, one phase-contrast image followed by one fluorescence image were acquired every 2.7 s for >5 min.

Phase contrast imaging was used to quantify the cumulated neuritic length (sum of all neurites for every neuron in the image) and the number of mobile objects (mitochondria and vesicles) inside neurons. The number of mobile objects per neuron was expressed as a function of the cumulated neuritic length (Fig. 5).

The video from fluorescence imaging was used to quantify the total number of mitochondria and the instant mitochondrial velocity. For this, the tip of moving mitochondria was manually pointed out on every image. The mean velocity was obtained by averaging all the instant velocities measured between two images for ~5 min (111 images, 110 instant velocities). The percentage of mitochondrial pause was obtained as the number of instant velocities equal to zero divided by the total number of instant velocities. The total number of mitochondria was determined on the first fluorescent image of the series and is expressed as a function of the cumulated neuritic length (Fig. 5). All parameters were estimated using Metamorph software.

Mitochondrial Calcium Retention Capacity (CRC)

Mitochondria were isolated from adult rat brains in order to obtain a large pool. Efforts were made to limit the number of rats used and a total of ten 3-month-old Sprague-Dawley female rats (230 ± 11 g, Charles Rivers, France) were required. All experiments were approved by the local ethics committee and were in full compliance with European community (EUVD 86/609/ EEC) guidelines for the care and use of laboratory animals. Rats were quickly euthanized by decapitation after a short anesthesia (4% isoflurane, IsoFlo, Axience, France). Brains were removed and rinsed in MSHE buffer (mannitol 225 mM, sucrose 75 mM, Hepes 10 mM, EGTA 1 mM, pH 7.4). Fore-brain tissue (without cerebellum) was homogenized in ice-cold

isolation buffer (MSHE + bovine serum albumin, 1 mg mL⁻¹) and mitochondria were isolated according to a previously described protocol (Rosenthal et al., 1987).

The mitochondrial protein concentration was quantified according to the method of Bradford (Quick start Bradford protein assay kit, Bio Rad, France). A reference of 1 mg mL⁻¹ of bovine serum albumin was used (Bradford, 1976).

The isolated mitochondria were diluted in CRC buffer (sucrose 250 mM, Tris-Mops 10 mM, Pi 1 mM, pH = 7.4) to a final concentration of 0.5 mg protein/mL and with 5 mM succinate (sodium succinate dibasic hexahydrate, Sigma–Aldrich, France) and 0.25 μM calcium green[®] probe (Calcium GreenTM-5N, hexapotassium salt, Molecular Probes, France). One minute after adding MnCl₂ to the mitochondria solution, the absorbance at 506 nm was recorded in real time with a spectrophotometer (Photon Technology International, PTI) until MPTP opening, obtained by adding Ca²⁺ (10 μM diluted in CRC buffer; 99%, Sigma–Aldrich, France) every minute until fluorescence dramatically increased. The same experiment was performed for 11 concentrations of MnCl₂ (0–200 μM), until total mitochondrial death (characterized by no fluorescence increase after Ca²⁺ addition). In addition, the MPTP reference inhibitor, 1 μM cyclosporine-A (CsA, Sigma–Aldrich, France), was added to the mitochondria solution in absence or in presence of MnCl₂ (50 μM).

The Ca²⁺ concentration (μM) required to open MPTP was calculated and expressed as a function of Mn²⁺ concentration (μM) in the medium.

Statistical Analysis

Results are expressed as mean ± standard error of the mean (SEM). All the comparisons are parametric unpaired *t* tests performed using Excel software.

To evaluate whether the sum of neuritic length is a predictor of the number of mobile objects in the phase contrast image, the Pearson correlation coefficient was computed. The same test was performed to evaluate whether the neuritic length is a predictor of the number of mitochondria.

A *P* value < 0.05 was considered as significant.

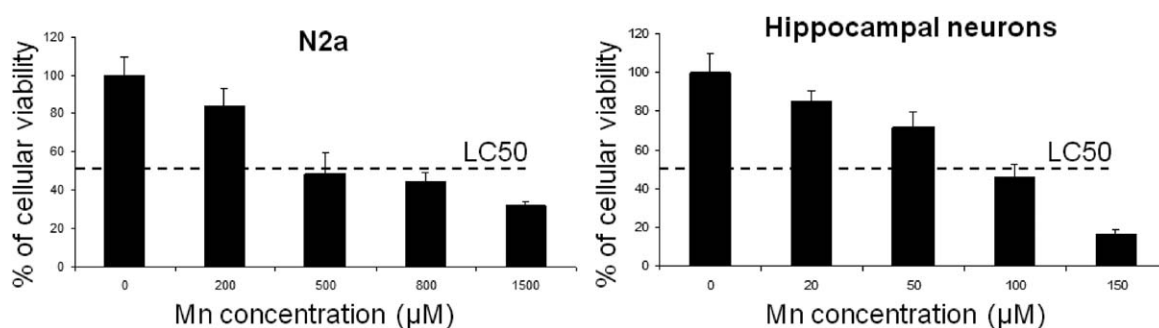


FIGURE 2. Survival of N2a cells and primary hippocampal neurons determined by MTT assay 24 h after administration of various concentrations of Mn²⁺. Survival is representative of five separate experiments for each cell type (mean ± SEM). The dashed line represents 50% cell survival.

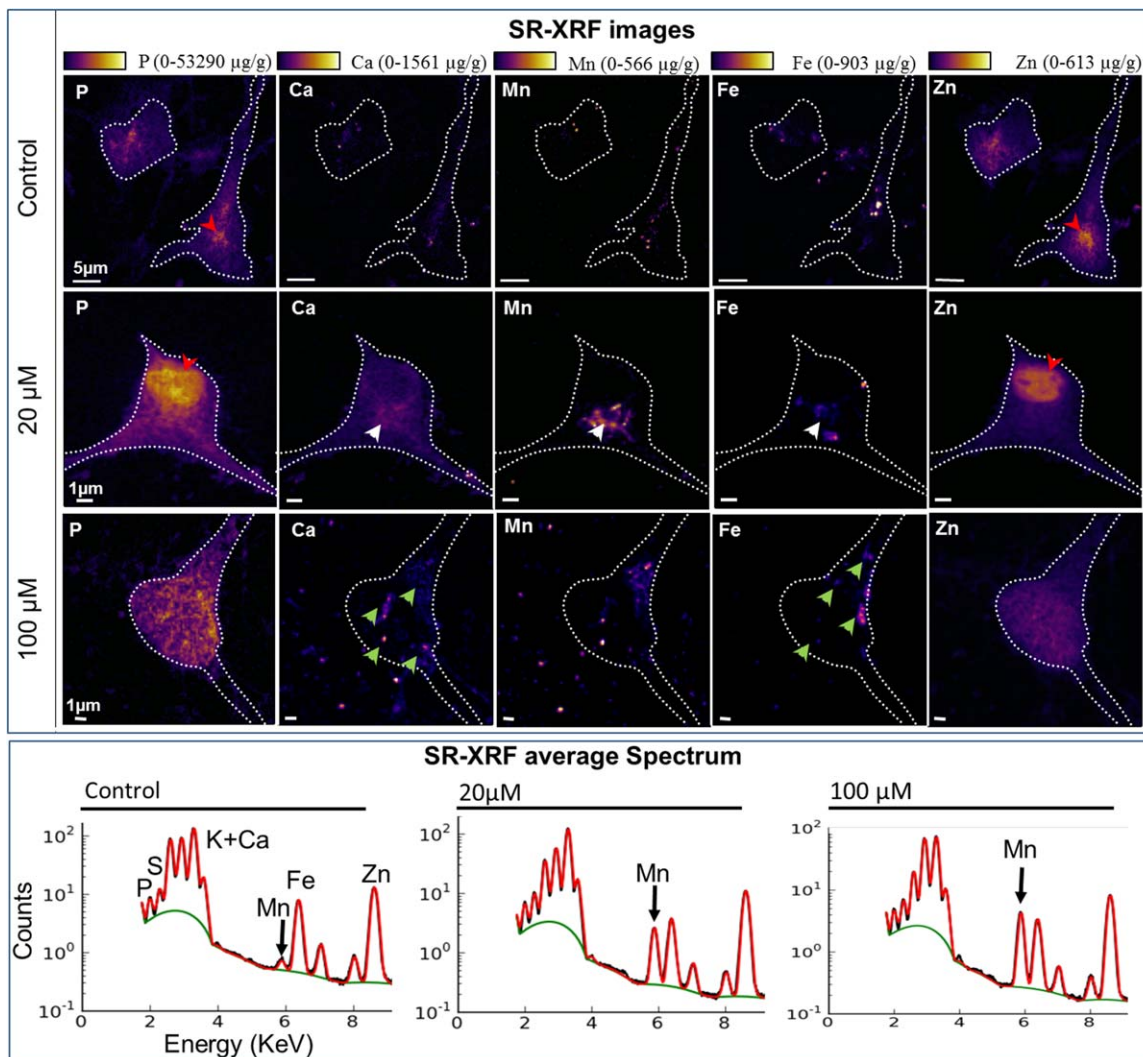


FIGURE 3. Map of metals distribution in hippocampal neurons obtained by SR-XRF. Two-dimensional elemental distribution of phosphorus, calcium, potassium, manganese, and zinc in HN 24 h after adding different concentrations of Mn²⁺ to the culture medium: 0 (control), 20, and 100 μM of Mn²⁺. Cell contours appear as a white dotted line (manually drawn from the P map). The color scale is in micrograms of element per g of dry weight (see also Table 1) and varies for each element (min and max values). Red arrowheads show P and Zn located in the cell nucleus;

white arrowheads point to Ca, Fe, and Mn distributed in the perinuclear area and green arrowheads show Ca and Fe redistribution in the cytoplasm. Normalized fluorescence spectra, averaged over the entire map, are represented in the right panel. The green line corresponds to the baseline and the red line to the fit across the data. An arrow points to the Mn peak for each condition. [Color figure can be viewed in the online issue, which is available at wileyonlinelibrary.com.]

RESULTS

Cell Dysfunction due to Mn²⁺ in Hippocampal Neurons and N2a Cells

The dysfunction of N2a and hippocampal neurons (HN), assessed with MTT 24 h after exposure to Mn²⁺, is expressed as a fraction of the number of viable cells in the untreated control and as a function of the administered MnCl₂ concentration (Fig. 2). This fraction decreased from 83.8% ± 9.4% (200 μM Mn²⁺) to 32.0% ± 1.9% (1,500 μM Mn²⁺) for N2a cells and from 85.0% ± 5.4% (20 μM Mn²⁺) to 16.3% ± 3.1% (150

μM Mn²⁺) for HN (Fig. 2). A straight line was fitted through the data (percentage of viable cells as a function of Mn²⁺ concentration) for N2a: $y = -0.04x + 87.97$, LC50 = 863 μM and for HN: $y = -0.54x + 98.46$, LC50 = 90 μM.

Distribution of Mn in Hippocampal Neurons and N2a Cells

In control HN (Fig. 3) and N2a cells (Supporting Information Fig. 1), the SR-XRF signal corresponding to Mn was low. Twenty-four hours after Mn²⁺ treatment (20 μM for HN; 600 μM for N2a), Mn concentration increased around 14-fold ($P < 0.0001$) and 12-fold ($P < 0.001$) in HN and N2a cells

TABLE 1.

Element Concentration of P, K, Ca, Fe, Cu, and Mn²⁺ in HN Cells Obtained by SR-XRF

Metals in HN	Control (µg g ⁻¹) (n = 18)	20 µM of Mn (µg g ⁻¹) (n = 11)	100 µM of Mn (µg g ⁻¹) (n = 15)
P	29,895 ± 5,460	37,060 ± 7,829**	34,176 ± 4,575*
K	23,516 ± 4,667	26,313 ± 5,217	27,117 ± 3,325*
Ca	66 ± 32	166 ± 56***	157 ± 76***
Fe	131 ± 35	96 ± 27**	122 ± 35
Cu	7.7 ± 4	5.6 ± 2	5.8 ± 1
Zn	168 ± 19	183 ± 23	179 ± 22
Mn	5.3 ± 1.5	77 ± 24***	248 ± 79***###

Concentrations of elements are expressed in micrograms of element per g of dry weight for each Mn²⁺ concentration (0 (Control), 20, and 100 µM). n = number of analyzed samples per condition.

Experiments were carried out on X-ray nanoprobe beamline (ID22NI) using incident energy of 17.5 keV. 20 and 100 µM of Mn²⁺ versus Control: *P < 0.05; **P < 0.01; ***P < 0.001 using parametric unpaired t tests. 20 versus 100 µM of Mn²⁺: ##P < 0.01; ###P < 0.001 (mean ± SEM) using parametric unpaired t tests.

respectively as compared to control (Tables 1 and 2). The Mn was found localized in perinuclear regions and appeared to accumulate in specific organelles. Importantly, the SR-XRF images reveal that Mn spots may also be distributed along neurites in HN (Supporting Information Fig. 2).

At a higher concentration of Mn²⁺ (100 µM for HN; 1,000 µM for N2a), the Mn concentration in HN and N2a further increased by about 47-fold (P < 0.0001) and 34-fold (P < 0.0001), respectively, as compared to control (Tables 1 and 2). Mn distribution then became more diffuse within the cytoplasm.

Phosphorus, Zinc, Calcium, and Iron Distribution in Hippocampal Neurons and N2a Cells

As shown in Figure 3 for HN and in Supporting Information Figure 1 for N2a, phosphorus (P) and zinc (Zn, not detected for N2a) were mostly found in the cell nucleus (red arrowheads), in agreement with the literature (Ortega et al., 2009). After adding a high concentration of Mn²⁺ to the culture medium, the distributions of P and Zn became much

more heterogeneous. In the control condition, Ca and Fe were barely detectable in HN and N2a cells whereas, at moderate Mn²⁺ concentrations (20 µM for HN; 600 µM for N2a), Ca and Fe were found distributed in the perinuclear, Mn²⁺ rich, region (white arrowheads) in HN. At higher Mn²⁺ concentrations (100 µM for HN; 1,000 µM for N2a), Ca and Fe were redistributed throughout the cytoplasm (green arrowheads). The exposition of HN to moderate (20 µM) and high (100 µM) concentrations of Mn²⁺, increased the concentration of P by about 24% (P < 0.01) and 14% (P < 0.05), respectively, as compared to the control condition. Similarly, compared to the control condition, Ca and K increased by about 140 to 150% (P < 0.001) and 15% (P < 0.05) respectively with 100 µM Mn²⁺, while Fe significantly decreased by 27% with 20 µM Mn²⁺. The distribution of Zn and Cu in HN displayed no change upon addition of Mn²⁺ (Table 1).

In N2a cells, both moderate and high concentrations of Mn²⁺ (600 and 1,000 µM, respectively) increased the amounts of Ca (by around 210 and 350%, respectively, P < 0.001) and Fe (by around 50%, P < 0.001 and 490%, P < 0.001, respectively). Finally, P and K dramatically increased (by 300 and

TABLE 2.

Element Concentration of P, K, Ca, Fe, Cu, and Mn²⁺ in N2a Cells Obtained by SR-XRF

Metals in N2a	Control (µg g ⁻¹) (n = 8)	600 µM of Mn (µg g ⁻¹) (n = 3)	1,000 µM of Mn (µg g ⁻¹) (n = 6)
P	10,305 ± 580	11,271 ± 2,836	41,089 ± 5,056***###
K	10,953 ± 1,313	13,773 ± 3,484	46,909 ± 3,686***###
Ca	38 ± 5	117 ± 32***	171 ± 30***
Fe	12 ± 2	18 ± 2**	70.5 ± 28***
Mn	5 ± 1.1	62 ± 18***	169 ± 26***###

Concentrations of elements are expressed in micrograms of element per g of dry weight for each Mn²⁺ concentration (0 (Control), 600, and 1,000 µM). n = number of analyzed samples per condition.

Control N2a experiments were carried out on X-ray nanoprobe beamline (ID22NI) using incident energy of 17.5 keV. N2a treated with Mn 600 and 1,000 µM were analyzed at ID21 end station using an X-ray incident energy of 7.2 keV. 600 and 1,000 µM of Mn²⁺ versus Control: *P < 0.05; **P < 0.01; ***P < 0.001 using parametric unpaired t tests. 600 versus 1,000 µM of Mn²⁺: ##P < 0.01; ###P < 0.001 (mean ± SEM) using parametric unpaired t tests.

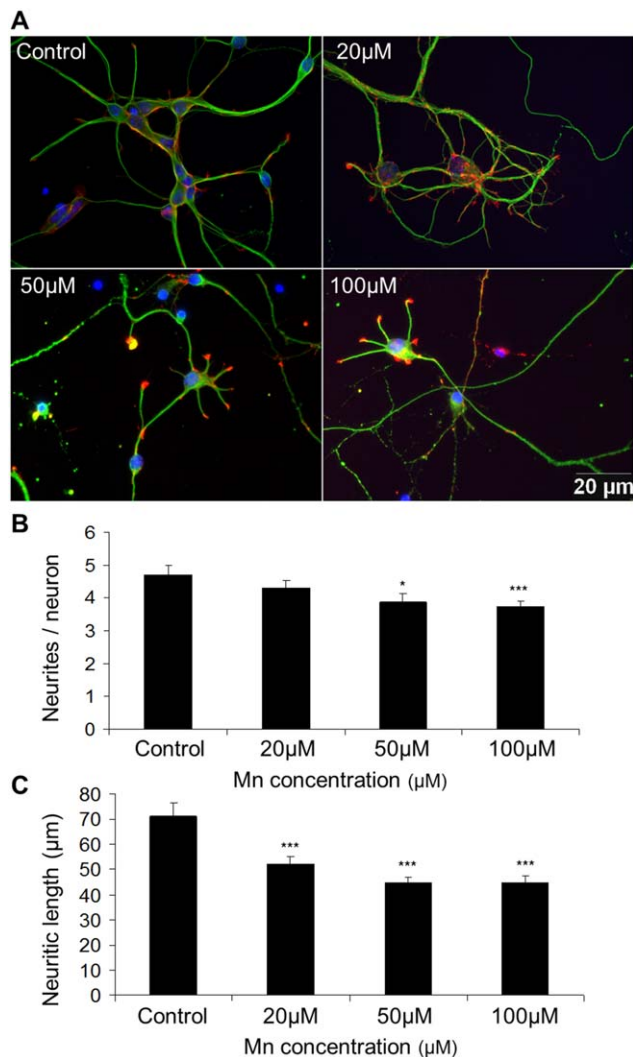


FIGURE 4. Impact of Mn^{2+} on the morphology of hippocampal neurons. After 48 h in culture, HN were exposed to Mn^{2+} for 24 h. Four concentrations of Mn^{2+} were used: 0 (control), 20, 50, and 100 μM . A. Immunofluorescence labeling. Neuronal fibrillar actin (red), tubulin (green) and nucleus (blue). The reduction in neuritic length as Mn^{2+} concentration increases is readily visible. B. Cumulated neuritic length. $n = 60$ per condition, * $P < 0.05$; *** $P < 0.001$ (mean \pm SEM) using parametric unpaired t tests. C. Number of neurites per neuron. [Color figure can be viewed in the online issue, which is available at wileyonlinelibrary.com.]

330%, respectively, $P < 0.001$) after 24-h exposure to 1,000 μM Mn^{2+} , with respect to control (Table 2).

Mn^{2+} Impact on Hippocampal Neuron Morphology

Immunostaining revealed increasing alterations of the cytoskeletal organization of neurites with increasing concentration of Mn^{2+} (from 50 to 100 μM ; Fig. 4). The number of neurites per neuron significantly decreased in the presence of high concentrations of $MnCl_2$ (around -17% , $P < 0.05$ vs. control

and -21% , $P < 0.001$ vs. control, in the presence of 50 and 100 μM Mn^{2+} in the medium, respectively). In addition, neuritic length significantly shortened with concentrations of Mn^{2+} above 20 μM (around -27% , -37% , and -37% in presence of 20, 50, and 100 μM Mn^{2+} in the medium, respectively; $P < 0.001$ vs. control for each), with an accumulation of actin at the neuritic extremities.

Mn^{2+} Impact on Mitochondria and Vesicle Dynamics in Hippocampal Neurons

The number of mobile objects detected on phase contrast images significantly correlated with the cumulated neuritic length in HN ($R^2 = 0.66$; $P < 0.05$; Fig. 5). In Figure 5B, HN in control conditions can be distinguished by their higher cumulated neuritic length from those treated with either 50 or 100 μM Mn^{2+} . The positive correlation between the number of mobile objects and the cumulated neuritic length would suggest that Mn^{2+} has no major impact on the mobile object density in HN.

Similarly, the number of mitochondria per HN detected with a MitoTracker Red CMXRos dye also significantly correlated with the cumulated neuritic length ($R^2 = 0.58$; $P < 0.0001$; Fig. 5C). This suggests that the mitochondria density was not affected by Mn^{2+} in our experimental conditions. Note that the trajectories of the moving mitochondria also seemed to be qualitatively unperturbed.

The average mitochondrial instant velocity determined by video-microscopy (data not shown) significantly decreased (around -42% , $P < 0.05$ vs. control) in the presence of 50 μM but not 100 μM Mn^{2+} (Fig. 5D). However, the percentage of mitochondrial pauses (see Methods section) significantly increased in the presence of 100 μM Mn^{2+} (around 57%, $P < 0.05$ vs. control).

Mn^{2+} Impact on Mitochondrial Calcium Retention Capacity (CRC)

The Ca concentration required for MPTP opening decreased as Mn^{2+} concentration increased ($R^2 = 0.903$; $P < 0.001$; Fig. 6). For example, in the presence of 50 μM Mn^{2+} , the CRC decreased by around 22% ($P < 0.001$) as compared to control. Note that the CRC became null at 200 μM Mn^{2+} . The MPTP reference inhibitor, CsA, significantly increased the CRC for 0 and 50 μM of Mn^{2+} (by around 30%, $P < 0.001$ vs. control for both conditions).

DISCUSSION

In this study, we have characterized the impact of Mn^{2+} on HN and differentiated N2a cells at the subcellular level and have demonstrated the differences in their response to Mn^{2+} exposure at concentrations above and below that inducing 50% lethality (LC50). Addition of Mn^{2+} at a

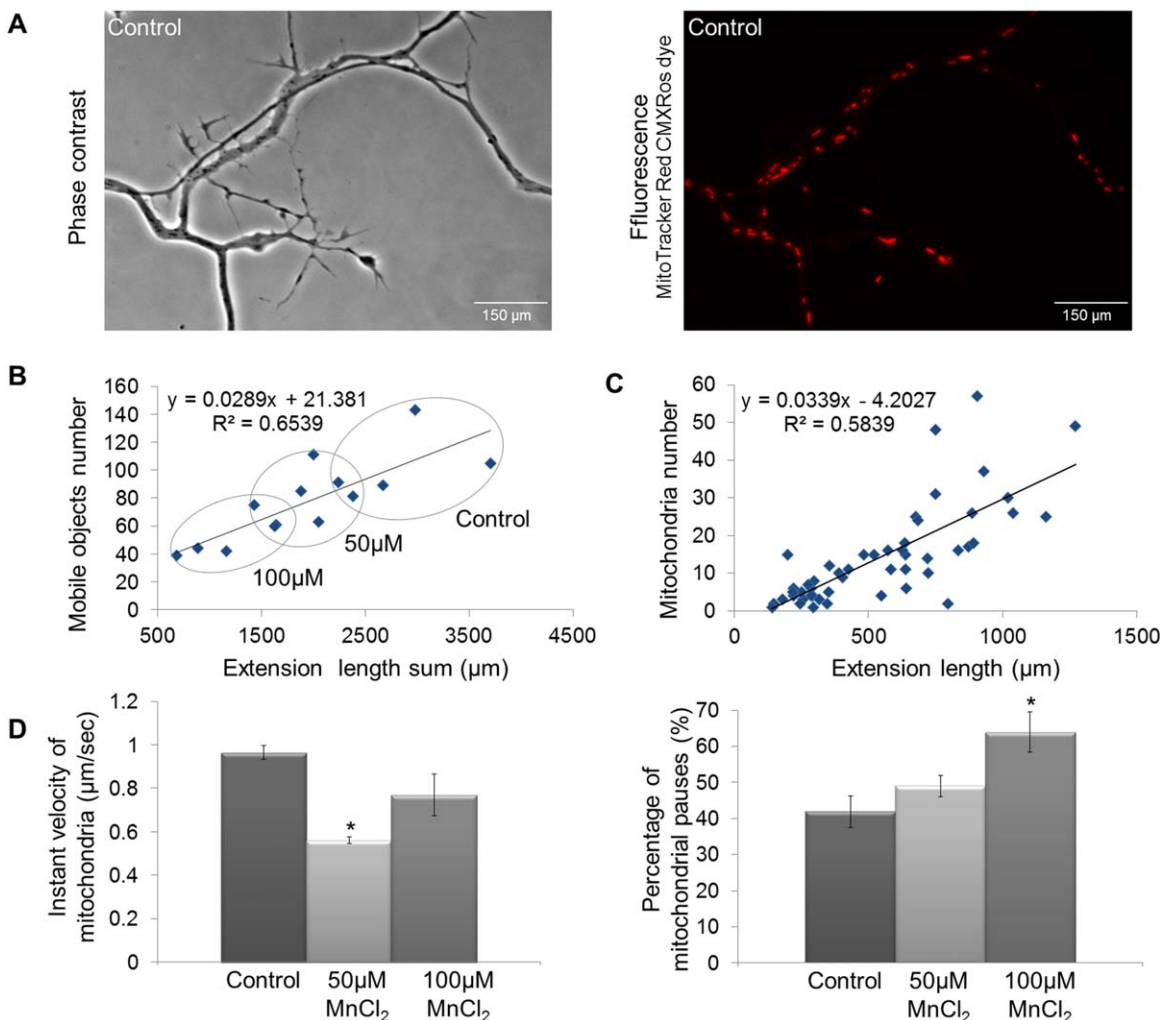


FIGURE 5. Impact of Mn^{2+} on the dynamics of mitochondria. After 48 h in culture, HN was exposed to Mn^{2+} for 24 h. Three concentrations of Mn^{2+} were used: 0 (control), 50, and 100 μM . A. Images of *in vitro* control HN. Left (phase contrast) and right (fluorescence; mitochondria appear in red) images were acquired using an $\times 100$ oil objective. B. Number of mobile objects (mitochondria and vesicles) as a function of neuritic length. Each point corresponds to the analysis of one image. The line represents a linear fit of the data. The three gray circles contour the points obtained for the three Mn^{2+} concentrations. C.

Number of mitochondria as a function of the cumulated neuritic length. Each point represents the analysis of one neurite. The line represents the linear fit to the data. D. Mean instant velocity of mitochondria ($\mu m s^{-1}$) and percentage of pauses (%) in the presence of 0, 50, or 100 μM Mn^{2+} . Control: $n = 20$; 50 μM of Mn^{2+} : $n = 16$; 100 μM of Mn^{2+} : $n = 5$, $*P < 0.05$ vs. control; (mean \pm SEM) using parametric unpaired t tests. [Color figure can be viewed in the online issue, which is available at wileyonlinelibrary.com.]

concentration below LC50 (20 μM for HN and 600 μM for N2a) led to a perinuclear distribution of Mn with mean Mn amounts of 77 and 62 $\mu g g^{-1}$ in HN and N2a cells, respectively. In contrast, addition of Mn^{2+} at a concentration above LC50 (100 μM for HN and 1,000 μM for N2a) led to a more diffuse distribution of Mn within the cytoplasm. SR-XRF also revealed that Mn occasionally accumulated in discrete, 200-nm large spots along HN neurites. In addition, we observed a decrease in mitochondrial motion at 50 μM Mn^{2+} with concomitant altered number of neurites per HN cell. Furthermore, Mn^{2+} induced a dose-dependent decrease in the calcium retention capacity (CRC) of isolated rat brain

mitochondria and induced mitochondrial death at a concentration of 200 μM .

Intracellular Mn Concentrations

The physiological concentration of Mn in the central nervous system is low (Aschner and Dorman, 2006) and using SR-XRF imaging, we previously reported a concentration of $2.5 \pm 1.6 \mu g g^{-1}$ in hippocampal tissue (Daoust et al., 2013) consistent with estimates obtained using particle-induced X-ray emission spectroscopy (Kemp and Danscher, 1979) and inductively coupled plasma mass spectrometry (Tarohda et al., 2004;

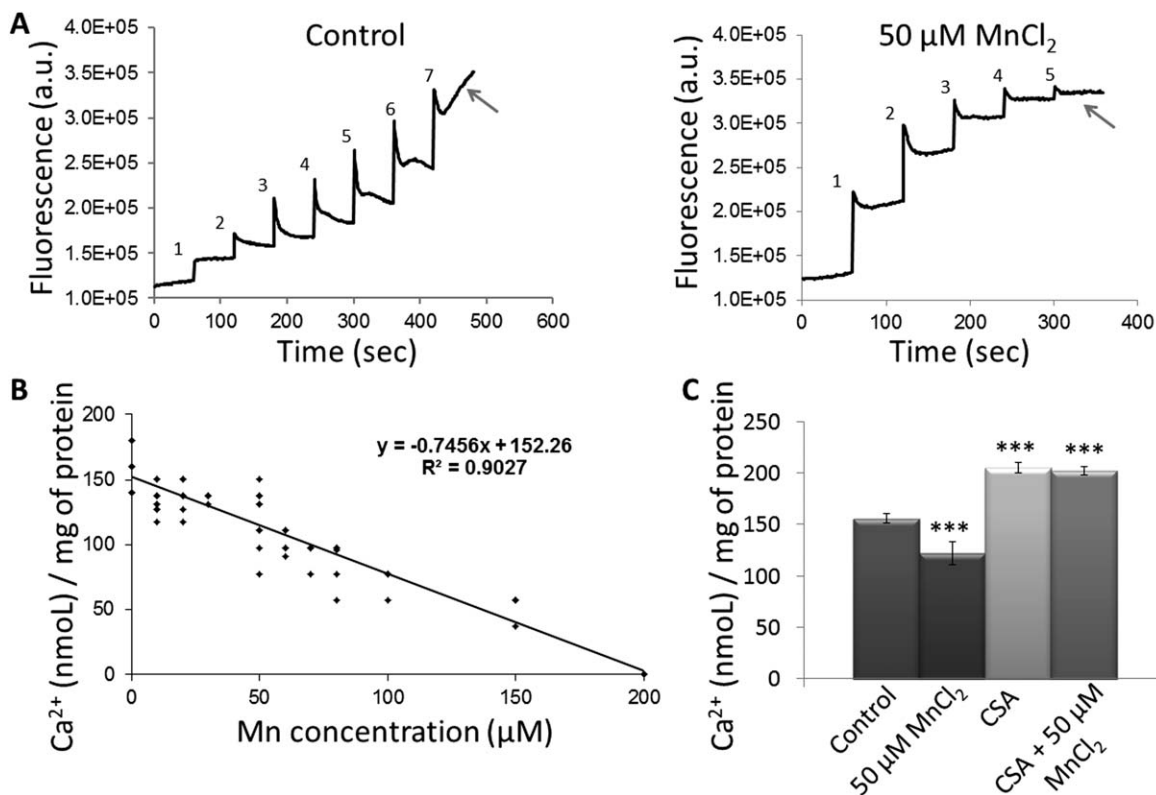


FIGURE 6. Impact of Mn^{2+} on calcium retention capacity (CRC) of isolated mitochondria. **A.** Calcium fluorescence curve as a function of time, for mitochondria in presence of 0 (control) and 50 μM of Mn^{2+} . The number of peaks decreases as the Mn^{2+} concentration increases. **B.** CRC as a function of Mn^{2+} concentra-

tion. The CRC decreases as the Mn^{2+} concentration increases in the culture medium ($P = 0.0004$). **C.** CRC in presence of cyclosporine-A (CsA, 1 μM), an inhibitor of the MPTP, with and without Mn^{2+} . $n = 10$ rats; *** $P < 0.001$ significantly different to control (unpaired t tests).

Bock et al., 2008). In this study, the physiological Mn concentration was measured to be around $5 \mu\text{g g}^{-1}$ for both cell types, slightly higher than that reported in PC12 cells (below $3 \mu\text{g g}^{-1}$, Carmona et al., 2010). However, Mn would seem to accumulate more in HN than in PC12 cells; addition of 100 μM Mn^{2+} for 24 h increased the intracellular concentration of Mn^{2+} in HN to $248 \pm 79 \mu\text{g g}^{-1}$ while 300 μM Mn^{2+} added for 24 h to PC12 cells increased Mn intracellular concentration to only $75 \pm 45 \mu\text{g g}^{-1}$ (Carmona et al., 2010). These differences in Mn^{2+} handling between neuron-like cells and primary neurons could arise from differences in the expression of metal transporters at the plasma membrane or intracellular membranes surrounding organelles (Yokel, 2009). For example, the expression of Mn-SOD differs between cell types: the concentration of Mn-SOD protein in N2a cells is fourfold that in HN (Cheng and Mattson, 1995; Chtourou et al., 2011). The results obtained in primary neurons may also depend on the age and on the origin of the neurons (cortex, mesencephalon, and hippocampus). Hernández et al. showed that the LC50 of Mn^{2+} increases with cell maturity from 27 μM in primary granular neurons to 180 μM in primary cortical neurons from mice fetuses after 120-h exposure (Hernández et al., 2011). The LC50 was demonstrated to have increased to above 400 μM for

primary cortical neurons obtained from rat neonates and for a 24-h exposure (Xu et al., 2009). Collectively, these results demonstrate that the sensitivity of neurons to Mn^{2+} depends on the neuronal type, their maturity, and on the duration of Mn^{2+} exposure.

The behavior of Mn^{2+} in cultured HN differs from that observed in rat brains. *In vivo*, 24 h after intracerebral injection of 10 μL of a 50 mM Mn^{2+} solution, Mn^{2+} concentration increases to $25 \mu\text{g g}^{-1}$ in hippocampal neurons (Daoust et al., 2013). *In vitro*, 24 h after addition of 20 μM Mn^{2+} to the culture medium, Mn concentration increased to $77 \mu\text{g g}^{-1}$. This suggests that neurons *in vivo* are exposed to Mn^{2+} concentrations lower than 20 μM and/or for shorter periods of time: a 24-h exposure to 10 μM would be sufficient to obtain a Mn concentration of $25 \mu\text{g g}^{-1}$. *In vivo* exposure of neurons to a Mn^{2+} concentration lower than the one injected could be ascribed to accumulation of Mn^{2+} in astrocytes. Indeed, 24 h after intracerebral injection of 10 μL of the 50 mM Mn^{2+} solution, we observed a Mn concentration of $105 \mu\text{g g}^{-1}$ (about 1,900 μM) in the hippocampal fissure, mainly composed of astrocytes (Daoust et al., 2013). Surprisingly, this is above the LC50 of Mn^{2+} for astrocytes measured by Giordano et al. ($\sim 1,000 \mu\text{M}$) (Giordano et al., 2009). Further

experiments on cocultures of neurons and astrocytes will be required to measure the temporal accumulation of Mn^{2+} in these two cell types.

Intracellular Distribution of Mn

SR-XRF imaging showed that Mn is mainly located in perinuclear areas in both N2a and HN exposed to moderate concentrations of Mn^{2+} . Addition of high concentrations of Mn^{2+} led to a more diffuse cytoplasmic distribution for both cell types, in agreement with the literature (Carmona et al., 2010; Sepúlveda et al., 2012; Dučić et al., 2013). In PC12 cells, Carmona et al. observed that Mn was preferentially localized in the Golgi apparatus after exposure to a moderate concentration of Mn^{2+} . Similarly, Dučić et al. showed Mn accumulation in the perinuclear area after a brief exposure of primary midbrain neurons to Mn^{2+} (500 μ M, 3 h; Dučić et al., 2013). In addition, SR-XRF imaging revealed, for the first time, discrete Mn spots along neurites in HN exposed to a moderate concentration of Mn^{2+} . This result supports previous assumptions of microtubular transport along microtubules within discrete subcellular compartments such as vesicles or mitochondria (Takeda et al., 1998; Culotta et al., 2005; Smith et al., 2007), the identification of which is, however, beyond the scope of this work.

To explain the cytoplasmic distribution of Mn, Carmona et al. proposed that the storage capacity of the Golgi apparatus, normally implicated in the cellular detoxification of Mn^{2+} , becomes overloaded in the presence of such toxic concentrations (Carmona et al., 2010). Sepúlveda et al. showed that a high concentration of Mn^{2+} inhibits the activity of secretory pathway Ca-ATPase (SPCA1), a Golgi pump regulating Ca^{2+} and Mn^{2+} homeostasis, and causes Golgi fragmentation in neurons and glia primary cultures (Sepúlveda et al., 2012). Such fragmentation could account for the more diffuse distribution of Mn observed in the cytoplasm after exposure to Mn^{2+} concentrations above the LC50. Mn^{2+} is also known to induce oxidative stress in the endoplasmic reticulum (Chun et al., 2001; Tjalkens et al., 2006; Seo et al., 2013). Indeed, Chun et al. described that a Mn^{2+} concentration above the LC50 in the SN4741 cell line (dopaminergic neuron-like), induces an endoplasmic reticulum stress response characterized by the activation of caspase-12 during apoptotic cell death. Mn^{2+} can also induce an alteration of endoplasmic reticulum calcium dynamics (Tjalkens et al., 2006). Overall, the observed Mn-rich perinuclear region could be assigned to the Golgi apparatus, to the endoplasmic reticulum, or to a combination of both.

This change in Mn distribution pattern, which may be used as a biomarker of Mn^{2+} toxicity on cells, may also affect the MR signal. Indeed, Mn^{2+} compartmentalization can modify the relaxivity (R1 and R2) of Mn^{2+} and thereby the MEMRI contrast (both qualitative and quantitative). According to Striijkers et al., a compartmentalization of Mn^{2+} inside the cell (cytoplasm and axon) could mask Mn^{2+} to water molecules and thus decrease its longitudinal relaxation rate constant R1 (Striijkers et al., 2009). *In vivo*, a concentration up to 5 μ g g^{-1}

of Mn in the tissue is detectable by MRI (Daoust et al., 2013) implying that MRI is able to detect physiological Mn in cells.

Mn^{2+} Impact on Ca, Fe, P, and K Homeostasis

Mn^{2+} is known to have a high affinity for Ca channels and Fe transporters (Aschner and Dorman, 2006). After exposure to Mn^{2+} , we observed that the Ca concentration increased in HN and N2a cells, in agreement with previous observations in primary cultured neurons (Xu et al., 2009). Such an increase in Ca was not observed in NGF-induced neuronal differentiated PC12 cells (Carmona et al., 2010). Considering the chemical similarity between Fe and Mn, Mn^{2+} was hypothesized to similarly alter the Fe homeostasis (Aschner, 2000; Carmona et al., 2010; Daoust et al., 2013). We indeed observed a decrease in Fe concentration in HN after Mn^{2+} exposure, in agreement with our observations in the rat hippocampus (Daoust et al., 2013). Conversely, in N2a cells, we observed an increase in Fe concentration after exposure to Mn^{2+} , in agreement with Abreo et al. (Abreo et al., 1999). Surprisingly, we observed a dramatic increase in P and K after exposure to Mn^{2+} that was not observed in PC12 cells or in hippocampal rat tissue (Carmona et al., 2010; Daoust et al., 2013). To our knowledge, these are the first results concerning the impact of Mn^{2+} on K and P homeostasis. An increase in extracellular K is described in hypoxia, ischemia and traumatic brain injury, in association with many different side effects such as widespread depolarization and disturbances in membrane-associated transport as well as in metabolic and synaptic neuronal function (Sugaya et al., 1975; Takahashi et al., 1980; Astrup et al., 1980). P is an important component of ATP that contributes towards the synthesis of proteins such as phosphocholine by phosphorylation. This increase in P and K concentrations could be the result of Mn toxicity on cell metabolism as shown by Zwingmann et al., 2004. This Mn^{2+} interaction with metal homeostasis can impact a number of cellular functions and thus could play a role in cellular death.

Mn^{2+} Impact on Hippocampal Neuron Morphology

We observed a dose-dependent decrease in the number and in the length of neurites after Mn^{2+} exposure. This effect has previously been reported and was ascribed to cellular stress (Vimard et al., 2011; Tiago et al., 2011). Similar results were obtained in primary neurons and astrocytes (Giordano et al. 2009; Sepúlveda et al., 2009) but not in PC12 cells (Lein et al., 2000). Overall, these results suggest that Mn^{2+} could alter neuronal connections. Mn does induce oxidative stress by liberation of reactive oxygen species (Graham, 1984) and lipid peroxidation which in turn prevents proper neuritic outgrowth. In PC12 cells, ascorbate was recently shown to reduce lipid peroxidation but not cell loss. Interestingly, ascorbate also reduces the oxidative-stress-mediated decrease of neuritic outgrowth in these cells (Slotkin and Seidler, 2010). However, in contrast to the situation *in vitro*, neuronal cell bodies and neurites are not entirely surrounded by

Mn²⁺ *in vivo*. Indeed, excess of Mn²⁺ in the brain primarily affects glial cell functions (Aschner et al., 1992).

Mn²⁺ Impact on Mitochondria Velocity and Calcium Retention Capacity

Several studies have suggested that intra-mitochondrial accumulation of Mn²⁺ in neurons plays a critical role in Mn²⁺ toxicity (Galvani et al., 1995; Zhang et al., 2003; Zwingmann et al., 2004). Here, we observed a decrease in the mean instant velocity of mitochondria in the presence of Mn²⁺. Note that the absence of a significant effect mediated by 100 μM Mn²⁺ is probably due to a bias in the analysis toward moving mitochondria. The fact that they display a significantly higher percentage of pauses in the presence of 100 μM than in the control condition reinforces this hypothesis. In any case, the shortening of neurites combined with a decreased velocity of mitochondria could be the result of a direct or indirect effect of Mn²⁺ on the interaction between mitochondria and microtubules.

The impact of Mn²⁺ on the respiratory chain is well documented (Husain et al., 1976; Galvani et al., 1995) and can lead to cell death (apoptosis). The opening of the MPTP is a critical stage of apoptosis in response to increased intracellular Ca²⁺ concentration (Halestrap et al., 2002; Morello et al., 2008). Our results suggest that Mn²⁺ facilitates this MPTP opening. Indeed, this effect was suppressed in the presence of CsA, an inhibitor of MPTP opening. All mitochondria died at concentrations up to 200 μM, which suggests a mitochondrial LC50 of about 100 μM, a value close to the measured LC50 of HN (90 μM).

Impact on *in vivo* MEMRI Experiments

In our attempt to emulate the concentrations of 50–100 mM used for intracerebral injections (Canals et al., 2008), we exposed cultured HN to Mn²⁺ concentrations ranging from 20 to 100 μM. Our results show that Mn²⁺ decreased mitochondrial velocity, length of neurites and facilitated MPTP opening. However, at a given Mn²⁺ concentration, the amount of Mn²⁺ measured was higher in cultured HN than *in vivo*, suggesting that our results may not be directly transposable *in vivo*. This discrepancy could be ascribed to astrocytes, which have the ability to accumulate Mn²⁺ and detoxify the brain after injection of Mn²⁺ (Vezér et al., 2007; Daoust et al., 2013; Sidoryk-Wegrzynowicz and Ashner, 2013). Nevertheless, our results do support the need to use the lowest possible Mn²⁺ concentrations in MEMRI experiments and optimize the MRI sequences to improve the sensitivity required to detect small concentrations of Mn²⁺.

CONCLUSION

In this study we have reported a number of new observations on the impact of Mn²⁺ on cultured hippocampal neurons. When cells are exposed to a concentration of Mn²⁺

below the LC50, Mn is preferentially localized around the nucleus, likely in the Golgi apparatus or in the endoplasmic reticulum, and in discrete spots in neurites. When neurons are exposed to a concentration of Mn²⁺ above the LC50, resulting in Mn²⁺ overload, the distribution of Mn becomes more diffuse within the cell, suggesting a mechanism of cell detoxification. Exposure of cultured HN to Mn²⁺ also induced a shortening of neurites, a decrease in the velocity of the mitochondria, and facilitated the MPTP opening. Altogether, these data support the use of primary neuronal cultures as a model to study Mn²⁺-induced toxicity on the brain. Future experiments should be performed on co-cultures of astrocytes and neurons to best mimic brain anatomical conditions.

Acknowledgments

The authors acknowledge the support of the MRI Facility of Grenoble (IRMaGe) and the ESRF Facility for provision of synchrotron radiation beamtime (respectively, exp. MD-458, MD-548). AD received a stipend from the Région Rhône-Alpes—Cluster HVN. The authors have no conflict of interest to declare. We thank the team from Surface Science Laboratory of the ESRF: A.Vial and F. Comin for AFM experiments. V. Hubert for assistance.

REFERENCES

- Abreo K, Abreo F, Sella ML, Jain S. 1999. Aluminum enhances iron uptake and expression of neurofibrillary tangle protein in neuroblastoma cells. *J Neurochem* 72:2059–2064.
- Aschner M. 2000. Manganese: Brain transport and emerging research needs. *Environ Health Perspect* 108:429–432.
- Aschner M, Dorman DC. 2006. Manganese: Pharmacokinetics and molecular mechanisms of brain uptake. *Toxicol Rev* 25:147–154.
- Aschner M, Gannon M, Kimelberg HK. 1992. Manganese uptake and efflux in cultured rat astrocytes. *J Neurochem* 58:730–735.
- Aschner M, Lukey B, Tremblay A. 2006. The manganese health research program (MHRP): Status report and future research needs and directions. *Neurotoxicology* 27:733–736.
- Astrup J, Rehnroona S, Siesjö BK. 1980. The increase in extracellular potassium concentration in the ischemic brain in relation to the preischemic functional activity and cerebral metabolic rate. *Brain Res* 199:161–174.
- Batandier C, Leverve X, Fontaine E. 2004. Opening of the mitochondrial permeability transition pore induces reactive oxygen species production at the level of the respiratory chain complex I. *J Biol Chem* 279:17197–17204.
- Bernardi P, Vassanelli S, Veronese P, Colonna R, Szabó I, Zoratti M. 1992. Modulation of the mitochondrial permeability transition pore. Effect of protons and divalent cations. *J Biol Chem* 267:2934–2939.
- Bock NA, Paiva FF, Nascimento GC, Newman JD, Silva AC. 2008. Cerebrospinal fluid to brain transport of manganese in a non-human primate revealed by MRI. *Brain Res* 1198:160–170.
- Bohic S, Cotte M, Salomé M, Fayard B, Kuehbachner M, Cloetens P, Martinez-Criado G, Tucoulou R, Susini J. 2012. Biomedical applications of the ESRF synchrotron-based microspectroscopy platform. *J Struct Biol* 177:248–258.

- Bradford MM. 1976. A rapid and sensitive method for the quantitation of microgram quantities of protein utilizing the principle of protein-dye binding. *Anal Biochem* 72:248–254.
- Canals S, Beyerlein M, Keller AL, Murayama Y, Logothetis NK. 2008. Magnetic resonance imaging of cortical connectivity in vivo. *NeuroImage* 40:458–472.
- Carmona A, Devès G, Ortega R. 2008. Quantitative micro-analysis of metal ions in subcellular compartments of cultured dopaminergic cells by combination of three ion beam techniques. *Anal Bioanal Chem* 390:1585–1594.
- Carmona A, Devès G, Roudeau S, Cloetens P, Bohic S, Ortega R. 2010. Manganese accumulates within golgi apparatus in dopaminergic cells as revealed by synchrotron X-ray fluorescence nanomapping. *ACS Chem Neurosci* 1:194–203.
- Cheng B, Mattson MP. 1995. PDGFs protect hippocampal neurons against energy deprivation and oxidative injury: Evidence for induction of antioxidant pathways. *J Neurosci* 15:7095–7104.
- Chtourou Y, Trabelsi K, Fetoui H, Mkannez G, Kallel H, Zeghal N. 2011. Manganese induces oxidative stress, redox state unbalance and disrupts membrane bound ATPases on murine neuroblastoma cells in vitro: Protective role of silymarin. *Neurochem Res* 36:1546–1557.
- Chun HS, Lee H, Son JH. 2001. Manganese induces endoplasmic reticulum (ER) stress and activates multiple caspases in nigral dopaminergic neuronal cells, SN4741. *Neurosci Lett* 316:5–8.
- Culotta VC, Yang M, Hall MD. 2005. Manganese transport and trafficking: Lessons learned from *Saccharomyces cerevisiae*. *Eukaryotic Cell* 4:1159–1165.
- Daoust A, Barbier EL, Bohic S. 2013. Manganese enhanced MRI in rat hippocampus: A correlative study with synchrotron X-ray microprobe. *NeuroImage* 64:10–18.
- De Jonge MD, Holzner C, Baines SB, Twining BS, Ignatyev K, Diaz J, Howard DL, Legnini D, Miceli A, McNulty I, Jacobsen CJ, Vogt S. 2010. Quantitative 3D elemental microtomography of *Cyclotella meneghiniana* at 400-nm resolution. *Proc Natl Acad Sci USA* 107:15676–15680.
- De Samber B, De Schampelaere KAC, Janssen CR, Vekemans B, De Rycke R, Martinez-Criado G, Tucoulou R, Cloetens P, Vincze L. 2013. Hard X-ray nanoprobe investigations of the subtissue metal distributions within *Daphnia magna*. *Anal Bioanal Chem* 405:6061–6068.
- Drapeau P, Nachshen DA. 1984. Manganese fluxes and manganese-dependent neurotransmitter release in presynaptic nerve endings isolated from rat brain. *J Physiol* 348:493–510.
- Dučić T, Barski E, Salome M, Koch JC, Bähr M, Lingor P. 2013. X-ray fluorescence analysis of iron and manganese distribution in primary dopaminergic neurons. *J Neurochem* 124:250–261.
- Erck C, Peris L, Andrieux A, Meissirel C, Gruber AD, Vernet M, Schweitzer A, Saoudi Y, Pointu H, Bosc C, Salin PA, Job D, Wehland J. 2005. A vital role of tubulin-tyrosine-ligase for neuronal organization. *Proc Natl Acad Sci USA* 102:7853–7858.
- Fitsanakis VA, Zhang N, Garcia S, Aschner M. 2010. Manganese (Mn²⁺) and iron (Fe): Interdependency of transport and regulation. *Neurotoxicity Res* 18:124–131.
- Galvani P, Fumagalli P, Santagostino A. 1995. Vulnerability of mitochondrial complex I in PC12 cells exposed to manganese. *Eur J Pharmacol Environ Toxicol Pharmacol* 293:377–383.
- Gibon J, Tu P, Bohic S, Richaud P, Arnaud J, Zhu M, Boulay G, Bouron A. 2011. The over-expression of TRPC6 channels in HEK-293 cells favours the intracellular accumulation of zinc. *Biochim Biophys Acta (BBA) Biomembr* 1808:2807–2818.
- Giordano G, Pizzurro D, VanDeMark K, Guizzetti M, Costa LG. 2009. Manganese inhibits the ability of astrocytes to promote neuronal differentiation. *Toxicol Appl Pharmacol* 240:226–235.
- Golub MS, Hogrefe CE, Germann SL, Tran TT, Beard JL, Crinella FM, Lonnerdal B. 2005. Neurobehavioral evaluation of rhesus monkey infants fed cow's milk formula, soy formula, or soy formula with added manganese. *Neurotoxicol Teratol* 27:615–627.
- Graham DG. 1984. Catecholamine toxicity: A proposal for the molecular pathogenesis of manganese neurotoxicity and Parkinson's disease. *Neurotoxicology* 5:83–95.
- Halestrap AP, McStay GP, Clarke SJ. 2002. The permeability transition pore complex: Another view. *Biochimie* 84:153–166.
- Hernández RB, Farina M, Espósito BP, Souza-Pinto NC, Barbosa F, Suñol C. 2011. Mechanisms of Manganese-induced neurotoxicity in primary neuronal cultures: The role of manganese speciation and cell type. *Toxicol Sci* 124:414–423.
- Heron P, Cousins K, Boyd C, Daya S. 2001. Paradoxical effects of copper and manganese on brain mitochondrial function. *Life Sci* 68:1575–1583.
- Higashi Y, Asanuma M, Miyazaki I, Hattori N, Mizuno Y, Ogawa N. 2004. Parkin attenuates manganese-induced dopaminergic cell death. *J Neurochem* 89:1490–1497.
- Husain R, Seth PK, Chandra SV. 1976. Early inhibition of succinic dehydrogenase by manganese in rat gonads. *Bull Environ Contam Toxicol* 16:118–121.
- Chandler JA, Morton MS. 1976. Determination of elemental area concentration in ultrathin specimens by X-ray microanalysis and atomic absorption spectrophotometry. *Anal Chem* 48:1316–1318.
- Josephs KA, Ahlskog JE, Klos KJ, Kumar N, Fealey RD, Trenerry MR, Cowl CT. 2005. Neurologic manifestations in welders with pallidal MRI T1 hyperintensity. *Neurology* 64:2033–2039.
- Kemp K, Danscher G. 1979. Multi-element analysis of the rat hippocampus by proton induced X-ray emission spectroscopy (phosphorus, sulfur, chlorine, potassium, calcium, iron, zinc, copper, lead, bromine, and rubidium). *Histochemistry* 59:167–176.
- Koretsky AP, Silva AC. 2004. Manganese-enhanced magnetic resonance imaging (MEMRI). *NMR Biomed* 17:527–531.
- Kwik-Urbe CL, Reaney S, Zhu Z, Smith D. 2003. Alterations in cellular IRP-dependent iron regulation by in vitro manganese exposure in undifferentiated PC12 cells. *Brain Res* 973:1–15.
- Lein P, Gallagher PJ, Amodeo J, Howie H, Roth JA. 2000. Manganese induces neurite outgrowth in PC12 cells via upregulation of alpha(v) integrins. *Brain Res* 885:220–230.
- Malecki EA. 2001. Manganese toxicity is associated with mitochondrial dysfunction and DNA fragmentation in rat primary striatal neurons. *Brain Res Bull* 55:225–228.
- Malthankar GV, White BK, Bhushan A, Daniels CK, Rodnick KJ, Lai JCK. 2004. Differential lowering by manganese treatment of activities of glycolytic and tricarboxylic acid (TCA) cycle enzymes investigated in neuroblastoma and astrocytoma cells is associated with manganese-induced cell death. *Neurochem Res* 29:709–717.
- Morello M, Canini A, Mattioli P, Sorge RP, Alimonti A, Bocca B, Forte G, Martorana A, Bernardi G, Sancesario G. 2008. Sub-cellular localization of manganese in the basal ganglia of normal and manganese-treated rats: An electron spectroscopy imaging and electron energy-loss spectroscopy study. *NeuroToxicology* 29:60–72.
- Narita K, Kawasaki F, Kita H. 1990. Mn²⁺ and Mg influxes through Ca channels of motor nerve terminals are prevented by verapamil in frogs. *Brain Res* 510:289–295.
- Olmsted JB, Carlson K, Klebe R, Ruddle F, Rosenbaum J. 1970. Isolation of microtubule protein from cultured mouse neuroblastoma cells. *Proc Natl Acad Sci USA* 65:129–136.
- Ortega R, Devès G, Carmona A. 2009. Bio-metals imaging and speciation in cells using proton and synchrotron radiation X-ray microspectroscopy. *J R Soc Interface* 6:S649–S658.
- Pautler RG. 2004. In vivo, trans-synaptic tract-tracing utilizing manganese-enhanced magnetic resonance imaging (MEMRI). *NMR Biomed* 17:595–601.

- Ponzoni S. 2012. Macrophages-mediated neurotoxic effects of intranigral manganese administration are attenuated by minocycline. *Neurosci Lett* 506:136–140.
- Rosenthal RE, Hamud F, Fiskum G, Varghese PJ, Sharpe S. 1987. Cerebral ischemia and reperfusion: Prevention of brain mitochondrial injury by lidoflazine. *J Cereb Blood Flow Metab* 7:752–758.
- Seo YA, Li Y, Wessling-Resnick M. 2013. Iron depletion increases manganese uptake and potentiates apoptosis through ER stress. *Neurotoxicology* 38:67–73.
- Sepúlveda MR, Vanoevelen J, Raeymaekers L, Mata AM, Wuytack F. 2009. Silencing the SPCA1 (secretory pathway Ca^{2+} -ATPase isoform 1) impairs Ca^{2+} homeostasis in the golgi and disturbs neural polarity. *J Neurosci* 29:12174–12182.
- Sepúlveda MR, Wuytack F, Mata AM. 2012. High levels of Mn^{2+} inhibit secretory pathway $\text{Ca}^{2+}/\text{Mn}^{2+}$ -ATPase (SPCA) activity and cause Golgi fragmentation in neurons and glia. *J Neurochem* 123:824–836.
- Sidoryk-Wegrzynowicz M, Aschner M. 2013. Role of astrocytes in manganese mediated neurotoxicity. *BMC Pharmacol Toxicol* 18:14–23.
- Silva AC, Bock NA. 2008. Manganese-enhanced MRI: An exceptional tool in translational neuroimaging. *Schizophrenia Bull* 34:595–604.
- Slotkin TA, Seidler FJ. 2010. Oxidative stress from diverse developmental neurotoxicants: Antioxidants protect against lipid peroxidation without preventing cell loss. *Neurotoxicol Teratol* 32:124–131.
- Smith KDB, Kallhoff V, Zheng H, Pautler RG. 2007. In vivo axonal transport rates decrease in a mouse model of alzheimer's disease. *NeuroImage* 35:1401–1408.
- Sole V, Papillon E, Cotte M, Walter P, Susini J. 2007. A multiplatform code for the analysis of energy-dispersive X-ray fluorescence spectra. *Spectrochim Acta B Atomic Spectrosc* 62:63–68.
- Stredrick DL, Stokes AH, Worst TJ, Freeman WM, Johnson EA, Lash LH, Aschner M, Vrana KE. 2004. Manganese-induced cytotoxicity in dopamine-producing cells. *NeuroToxicology* 25:543–553.
- Strijkers GJ, Hak S, Kok MB, Springer CS, Nicolay K. 2009. Three-compartment T1 relaxation model for intracellular paramagnetic contrast agents. *Magn Reson Med* 61:1049–1058.
- Sugaya E, Takato M, Noda Y. 1975. Neuronal and glial activity during spreading depression in cerebral cortex of cat. *J Neurophysiol* 38:822–841.
- Takahashi H, Manaka S, Sano K. 1981. Changes in extracellular potassium concentration in cortex and brain stem during the acute phase of experimental closed head injury. *J Neurosurg* 55:708–717.
- Takeda A, Kodama Y, Ishiwatari S, Okada S. 1998. Manganese transport in the neural circuit of rat CNS. *Brain Res Bull* 45:149–152.
- Tarohda T, Yamamoto M, Amamo R. 2004. Regional distribution of manganese, iron, copper, and zinc in the rat brain during development. *Anal Bioanal Chem* 380:240–246.
- Tiago T, Marques-da-Silva D, Samhan-Arias AK, Aureliano M, Gutierrez-Merino C. 2011. Early disruption of the actin cytoskeleton in cultured cerebellar granule neurons exposed to 3-morpholinosydnonimine-oxidative stress is linked to alterations of the cytosolic calcium concentration. *Cell Calcium* 49:174–183.
- Tjalkens RB, Zoran MJ, Mohl B, Barhoumi R. 2006. Manganese suppresses ATP-dependent intercellular calcium waves in astrocyte networks through alteration of mitochondrial and endoplasmic reticulum calcium dynamics. *Brain Res* 1113:210–219.
- Vezer T, Kurunzi A, Náray M, Papp A, Nagymajtényi L. 2007. Behavioral effects of subchronic inorganic manganese exposure in rats. *Am J Ind Med* 50:841–852.
- Vimard F, Saucet M, Nicole O, Feuilloley M, Duval D. 2011. Toxicity induced by cumene hydroperoxide in PC12 cells: Protective role of thiol donors. *J Biochem Mol Toxicol* 25:205–215.
- Xu B, Xu Z-F, Deng Y. 2009. Effect of manganese exposure on intracellular Ca^{2+} homeostasis and expression of NMDA receptor subunits in primary cultured neurons. *NeuroToxicology* 30:941–949.
- Yokel RA. 2009. Manganese flux across the blood-brain barrier. *Neuromol Med* 11:297–310.
- Zhang S, Zhou Z, Fu J. 2003. Effect of manganese chloride exposure on liver and brain mitochondria function in rats. *Environ Res* 93:149–157.
- Zwingmann C, Leibfritz D, Hazell AS. 2004. Brain energy metabolism in a sub-acute rat model of manganese neurotoxicity: An ex vivo nuclear magnetic resonance study using [1- ^{13}C]glucose. *Neurotoxicology* 25:573–587.